

Scaling up Deep Learning for PDE-based Models

Philipp Hähnel*

Jakub Mareček
Fearghal O'Donncha

Julien Monteil

August 12, 2021

Abstract

In numerous applications, forecasting relies on numerical solvers for partial differential equations (PDEs). Although the use of deep-learning techniques has been proposed, the uses have been restricted by the fact the training data are obtained using PDE solvers. Thereby, the uses were limited to domains, where the PDE solver was applicable, but no further.

We present methods for training on small domains, while applying the trained models on larger domains, with consistency constraints ensuring the solutions are physically meaningful even at the boundary of the small domains. We demonstrate the results on an air-pollution forecasting model for Dublin, Ireland.

1 Introduction

Solving partial differential equations (PDEs) underlies much of applied mathematics and engineering, ranging from computer graphics and financial pricing, to civil engineering and weather prediction. Conventional approaches to prediction in PDE models rely on numerical solvers and require substantial computing resources in the model-application phase. While in some application domains, such as structural engineering, the longer run-times may be acceptable, in domains with rapid decay of value of the prediction, such as weather forecasting, the run-time of the solver is of paramount importance.

In many such applications, the ability to generate large volumes of data facilitates the use of surrogate or reduced-order models [1] obtained using deep artificial neural networks [2]. Although the observation that artificial neural networks could be applied to physical models is not new [3, 4, 5, 6, 7, 8, 9, 10], and indeed, it is seen as one of the key trends [11, 12, 13] on the interface of applied mathematics, data science, and deep learning, their applications did not reach the level of success observed in the field of the image classification, speech recognition, machine translation, and other problems processing unstructured high-dimensional data, yet. A key issue faced by applications of deep-learning techniques to physical models is their scalability.

Even very recent research on deep-learning for physical models [14, 15, 16] uses a solver for PDEs to obtain hundreds of thousands of outputs. The deep learning can then be seen as means of non-linear regression between the inputs and outputs. For example, [15] have recently observed a factor of 12,000 computational speedup compared to that of a leading solver for the PDE, on

*All authors were with IBM Research – Ireland, in Damastown Industrial Park, Mulhuddart, Dublin 15, Ireland, while doing the research. Philipp and Jakub would like to thank the Institute of Pure and Applied Mathematics (IPAM), where this work has been finished, for the most kind hospitality.

the largest domain they were able to work with. Considering the PDE solver is used to generate the outputs to train the deep-learning model on, however, the deep-learning model is limited to the domain and application that it is trained on.

We present methods for training Deep Neural Networks (DNNs) on small domains, while applying the trained models on larger domains, with consistency constraints ensuring the solutions are physically meaningful even at the boundaries of the small domains. Our contributions are as follows:

- definition of the consistency constraints, wherein the output for one (tile of a) mesh is used to constrain the output for another (tile of a) mesh.
- methods for applying the consistency constraints within the training of a DNN, which allows for an increase in the extent of the spatial domain by concatenating the outputs of several PDE-based models by considering boundary conditions and state at the boundary.
- a numerical study of the approach on a pollution-forecasting problem, wherein we show the mean absolute percentage error (MAPE) of 3 per cent with respect to the pollution levels.

We note that the methods can be applied both in terms of “patching” multiple (tiles of a) meshes, and in terms of “zooming” in multi-resolution approaches, where lower-resolution (e.g., city-, country-scale) component constrains higher-resolution components (e.g., district-, city-scale), which in turn impose consistency constraints on the former.

2 Our Approach

Our work is a first attempt to apply techniques based on domain decomposition to deep learning. Conceptually, it promises the ability to concatenate outputs from disparate PDE-based simulation models into a single dataset for training deep learning with constraints to ensure consistency across the boundaries of the disparate simulations, i.e., physical viability across multiple meshes for a physical phenomenon governed by a PDE. The approach under consideration is rather intuitive and consists of training a deep learning model for each available sub-grid, providing a method to ensure consistency across sub-grids, and scaling up to the wider area such that the accuracy of the predictions is increased. Further, by enabling communication between meshes (via constraints), individual domain prediction can be provided with information external to the domain.

Let us consider an index-set \mathcal{M} of meshes $M_m, m \in \mathcal{M}$, with sets of n_m mesh points $P(M_m)$. The output of each PDE-based simulation on such a mesh consists of values in \mathbb{R}^{d_m} at each point of $P(M_m)$. Often, a small sub-set of $n_m^{(r)}$ of such points is of particular interest, which we call receptors $R(M_m)$; the remainder of the points represents hidden points $H(M_m)$. The receptors and hidden points thus partition the mesh points $P(M_m) = H(M_m) \cup R(M_m)$, with $n_m = n_m^{(h)} + n_m^{(r)}$. Further, let us consider the index-set $\mathcal{B} \subseteq \mathcal{M} \times \mathcal{M}$ of boundaries B_{mn} of meshes. Such a possibly infinite boundary $B_{mn} \subseteq P(M_m) \times P(M_n)$ links pairs of points from the two meshes. To each boundary B_{mn} we associate a constant ϵ_{mn} that reflects the importance of this boundary. Further, for each mesh M_m we have an ordered set of simulations indexed with time $t \in \mathbb{Z}$, where each simulation is defined by the inputs $x_t^{(m)} \in X_t^{(m)}$ and a set of outputs $y_t^{(m)} \in (\mathbb{R}^{d_m})^{n_m}$. Often, one wishes to consider $y_t^{(m)}$ being part of $x_{t+k}^{(m)}$ for some $k > 0$, in a recurrent fashion.

Our aim is to minimise residuals subject to consistency constraints to ensure physical “sanity” of the results, i.e.,

$$\begin{aligned}
 r^* &= \min_f \sum_t \sum_{m \in \mathcal{M}} \left\| \text{proj}_{R(M_m)} \left(y_t^{(m)} - f^{(m)}(x_t^{(m)}) \right) \right\| \\
 \text{s. t. } &\forall t \forall (m, n) \in \mathcal{B} \forall (p_1, p_2) \in B_{mn} : \\
 &\text{prox} \left(\text{proj}_{\{p_1\}} f^{(m)}(x_t^{(m)}) , \text{proj}_{\{p_2\}} f^{(n)}(x_t^{(n)}) \right) \leq \epsilon_{mn} ,
 \end{aligned} \tag{1}$$

where $\text{proj}_Q : (\mathbb{R}^{d_m})^{\times n_m} \rightarrow (\mathbb{R}^{d_m})^{\times |Q|}$ is a projection operator that projects the array of outputs at all points onto the outputs at a subset of points $Q \subset P(M_m)$, prox is a proximity operator, the decision variable defines the mapping $f = \{f^{(m)}\}_{m \in \mathcal{M}}$, whereby $f^{(m)}(x_t^{(m)})$ represents the output of a non-linear mapping between inputs and PDE-based simulation outputs at the points of the mesh, $f^{(m)} : X_t^{(m)} \rightarrow (\mathbb{R}^{d_m})^{\times n_m}$, on each independent mesh M_m , which can be seen as a non-linear regression, and ϵ_{mn} is a constant specific to $(m, n) \in \mathcal{B}$. We provide examples of $f^{(m)}$ in the following sections. The requirement of physical “sanity” is usually a statement about smoothness of the values of the mapping $f^{(m)}$ across the boundaries of two different meshes. To be able to compare those values, we require that the dimensions are the same, that is $\forall m, n \in \mathcal{M} : d_m = d_n \equiv d$. For example, for prox being the norm of a difference of the arguments, “smooth” at a point at the boundary of two meshes means that the values predicted within the two meshes at that point are numerically close to each other. Also adding the norm of the difference of their gradients to that makes it a statement about the closeness of their first derivatives too. Technically, “smoothness” is a statement about all their higher derivatives as well, however, we will only concern ourselves with their values, or zeroth order of derivatives, for now. Notice though that generically this is an infinitely large problem.

In theory, equation 1 can be solved by Lagrangian relaxation techniques, e.g., by solving:

$$r^* = \inf_{f, \lambda} \sum_t \left(\sum_{m \in \mathcal{M}} \left\| \text{proj}_{R(M_m)} \left(y_t^{(m)} - f^{(m)}(x_t^{(m)}) \right) \right\| \right. \\ \left. + \sum_{(m, n) \in \mathcal{B}} \sum_{(p_1, p_2) \in B_{mn}} \lambda_t^{(m)} \text{prox} \left(\text{proj}_{\{p_1\}} f^{(m)}(x_t^{(m)}) , \text{proj}_{\{p_2\}} f^{(n)}(x_t^{(n)}) \right) \right), \quad (2)$$

for $\lambda = \{\lambda_t^{(m)}\}_{t \in \mathbb{Z}}^{m \in \mathcal{M}}$. This can be seen as a statement that there exist $\lambda_t^{(m)}$, $t \in \mathbb{Z}$, such that the infimum over $f^{(m)}$ coincides with r^* , for each $m \in \mathcal{M}$. Clearly, if at least some of the boundaries B_{mn} are infinite, then the optimisation problem is infinite-dimensional.

Further, one can borrow techniques from iterative solution schemes in the numerical analysis domain. Notice that the first term in equation 2 is finite-dimensional and separable across the meshes. For each mesh M_m , $m \in \mathcal{M}$, the above can be computed independently. Further, one can sub-sample the boundaries to obtain a consistent estimator. Subsequently, one could solve the finite-dimensional projections of equation 2, wherein each new solution will increase the dimension of $\lambda_t^{(m)}$. While this is feasible in theory, the inclusion of non-separable terms with $\lambda_t^{(m)}$ would still render the solver less than practical.

Instead, we propose an iterative scheme, which is restricted to separable approximations. Let us imagine that during iteration k and at time t for a pair of points $(p_1, p_2) \in B_{mn}$ on the boundary indexed with $(m, n) \in \mathcal{B}$, we obtain values from the trained model at those points in the respective mesh, $\mathbb{R}^d \ni f_{p_1, t}^{(m)} = \text{proj}_{\{p_1\}} f^{(m)}(x_t^{(m)})$ and $\mathbb{R}^d \ni f_{p_2, t}^{(n)} = \text{proj}_{\{p_2\}} f^{(n)}(x_t^{(n)})$. While the two points p_1, p_2 lay in two different meshes, we would like the model outputs at those points to eventually coincide for high enough k . For that we iteratively construct vectors $\underline{\chi}_{p_1, p_2}^{(k+1)}$ and $\bar{\chi}_{p_1, p_2}^{(k+1)} \in \mathbb{R}^d$ during the k^{th} iteration that serve as lower and upper bounds on the values obtained from the training of $f^{(m)}$ during the next iteration. Those vectors can be updated through a variety of methods, two of the most naïve ones we discuss in the appendix A. In order to obtain convergence properties in a non-convex setting, we use an asymptotically vanishing shift term to adjust the interval according to the newly trained data, and a gradient term, according to

$$\underline{\chi}_{p_1, p_2}^{(k+1)} = \underline{\chi}_{p_1, p_2}^{(k)} + \frac{\kappa}{\sqrt{k} + \zeta} \left(\min \left(f_{p_1, t}^{(m)}, f_{p_2, t}^{(n)} \right) - \underline{\chi}_{p_1, p_2}^{(k)} \right) + \frac{\kappa \sqrt{k}}{\sqrt{k} + \zeta} \left(\underline{\chi}_{p_1, p_2}^{(k)} - \underline{\chi}_{p_1, p_2}^{(k-1)} \right), \\ \bar{\chi}_{p_1, p_2}^{(k+1)} = \bar{\chi}_{p_1, p_2}^{(k)} + \frac{\kappa}{\sqrt{k} + \zeta} \left(\max \left(f_{p_1, t}^{(m)}, f_{p_2, t}^{(n)} \right) - \bar{\chi}_{p_1, p_2}^{(k)} \right) + \frac{\kappa \sqrt{k}}{\sqrt{k} + \zeta} \left(\bar{\chi}_{p_1, p_2}^{(k)} - \bar{\chi}_{p_1, p_2}^{(k-1)} \right). \quad (3)$$

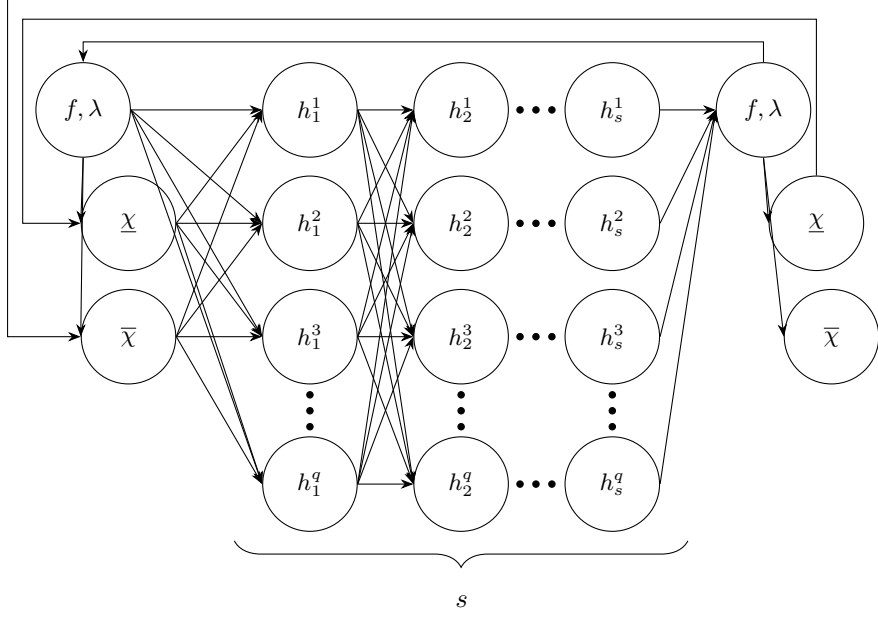


Figure 1: A schematic illustration of our recurrent neural network, where the recursion considers the consistency constraints defined by $\underline{\chi}, \bar{\chi}$.

The free parameters κ and ζ are tunable parameters of the model and resemble learning rates. In principle, they could be chosen dynamically and also depend on the boundary (m, n) . Choosing them to be constants eases the computational efforts however. For the first iterations, the boundary values are initialised using the minimum and maximum of the labels, respectively. We can now form univariate interval constraints, restricting the corresponding elements of both $f^{(m)}$ at p_1 and $f^{(n)}$ at p_2 of the next iteration to the respective interval $(\underline{\chi}_{p_1, p_2}, \bar{\chi}_{p_1, p_2})$. Notice that replacing $\lambda_t^{(m)}$ with a constant λ provides an upper bound on r^* , which is computationally much easier to solve.

In the scheme, we consider a finite-dimensional projection of equation 2. For each $(m, n) \in \mathcal{B}$ we consider a finite sample $\hat{B}_{mn} \subset B_{mn}$ of pairs of points, for which we obtain

$$r^* = \min_{f, \lambda} \sum_t \left(\sum_{m \in \mathcal{M}} \left\| \text{proj}_{R(M_m)} (y_t^{(m)} - f^{(m)}(x_t^{(m)})) \right\| \right. \\ \left. + \sum_{\substack{(m, n) \in \mathcal{B} \\ (p_1, p_2) \in \hat{B}_{mn}}} \sum_{\substack{l \in (m, p_1) \\ p \in (n, p_2)}} \epsilon_{mn} \lambda \left\| \max(0, \underline{\chi}_{p_1, p_2} - f_{p, t}^{(l)}) + \max(0, f_{p, t}^{(l)} - \bar{\chi}_{p_1, p_2}) \right\|_1 \right), \quad (4)$$

where we consider the function $\max : \mathbb{R} \times \mathbb{R}^d \rightarrow \mathbb{R}^d$ to operate element-wise. Further, when we consider λ as a hyperparameter, we obtain an optimisation problem separable in $m \in \mathcal{M}$, which in the limit of $|\hat{B}_{mn}| \rightarrow |B_{mn}|$ provides an over-approximation for any λ .

In deep learning, this scheme should be seen as a recurrent neural network (RNN). A fundamental extension of RNN compared to traditional neural network approaches is parameter sharing across different parts of the model. We refer to [2, Chapter 10] for an excellent introduction and Figure 1 for a schematic illustration. Each run provides constants $(\underline{\chi}_{p_1, p_2}, \bar{\chi}_{p_1, p_2})$, which are used in the consistency constraints of the subsequent run.

In terms of training the RNN, it is important to notice that equation 4 allows for very fast convergence rate even in many classes of non-linear maps f . For instance, when $f^{(m)} : X_t^{(m)} \rightarrow$

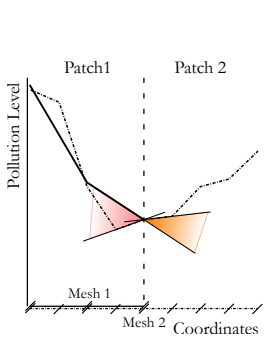


Figure 2: Discrete gradients: sub-differentials between predictions using two different meshes.

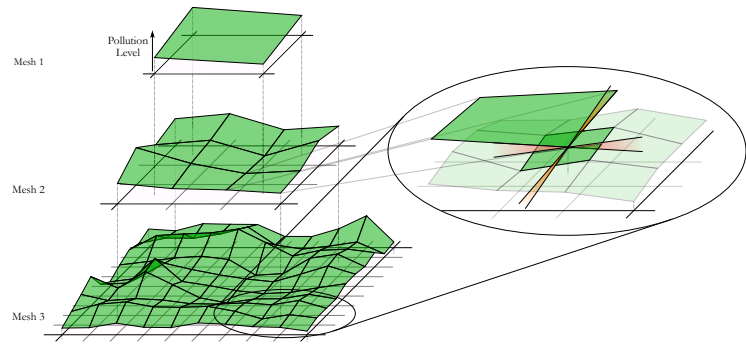


Figure 3: Changing the resolution of meshes imposes consistency constraints on the values and two-dimensional sub-differentials between predictions. Shown is the transition between three meshes of different resolution and the potential difference between the sub-differentials of figure 2.

$(\mathbb{R}^{d_m})^{n_m}$ is a polynomial of a fixed degree [17], then equation 4 is strongly convex, despite the max function making it non-smooth. The subgradient of the max function is well understood [18] and readily implemented in major deep-learning frameworks. Even in cases, when the resulting problem is not convex, one could consider convexifications, following [19].

In numerical analysis, in general, and with respect to the multi-fidelity methods [20], in particular, our approach could be seen as iterative model-order reduction. The original PDEs could be seen as the full-order model (FOM) to reduce, and equation 1 could be seen as a high-fidelity data-fit reduced-order model (ROM), albeit not a very practical one, whereas equation 4 could then be seen as a low-fidelity data-fit ROM, which allows for rapid prediction.

In learning theory, it is well known since the work of [21] that even a feed-forward network with three or more layers of a sufficient number of neurons (e.g., with sigmoidal activation function) allows for a universal approximation of functions on a bounded interval. It is not guaranteed, however, that the approximation has any further desirable properties, such as energy conservation etc. Our consistency constraints allow for such properties.

Fundamentally, the approach can be summarised as learning the non-linear mapping between inputs and predictions on each independent mesh, and iterating to ensure consistency of the solution across meshes. Such an approach draws on a long history of work on setting boundary conditions as consistency constraints in the solution of PDEs [22]. It can be applied to not only the simple patching of two tiles, but also when changing the resolution of the mesh. We use the term patching for working with neighbouring meshes at a single resolution and zooming when the mesh resolution changes. As we discussed earlier, ensuring “smoothness” involves not only bounds on the values at the boundaries, but also on their higher gradients, or sub-differentials. Since this is not part of our actual implementation, we will not go further into detail, however, we provide figures 2 and 3, were the sub-differentials for both patching and zooming are illustrated.

3 Methods

To illustrate this framework, we train the Recurrent Neural Network for city-scale pollution monitoring, utilising:

- The 3D structure of the atmosphere from our numerical weather forecasting model comprising

the full atmospheric data (i.e., velocities, pressures, humidity, and temperatures in 3D).

- Pollution measurements and traffic data, since traffic is measurable and strongly correlated to (esp. nitrogen oxide, particulate matter) pollution in the cities.
- The given discretisation of a city in multiple meshes, corresponding to multiple geographic areas with their specificities.

Our test case is based in the city of Dublin, Ireland, for which real-time streams of traffic and pollution data (from Dublin City Council), and weather data (from the Weather Company) are available to us, but which did not have any large-scale models of air pollution deployed.

3.1 Air pollution-based Forecasting

Air pollution is known to have significant health impacts [23]. Typically, in cities, traffic-induced pollution is measured via the levels of nitrogen oxides (NOx) and Particulate Matter (PM). The contribution of traffic to the levels of NOx is known to be around 70% in European cities, whereas the contribution of traffic to the levels of particulate matter pollution is known to be up to 50% in cities of OECD countries, in particular due to the heavy presence of diesel engines.

We aim at estimating and predicting the traffic-induced air pollution levels of NO₂ (which is closely related to NOx), PM2.5 and PM10, for defined receptors across the city. An air pollution dispersion model propagates the pollution levels emitted from the roadway links (line sources). The PDE-based model that we are using is based on the Gaussian Plume model, studied at least since the work of [24], and (by now) a standard model in describing the steady-state transport of pollutants. The data inputs are the periodic traffic volumes for a number of roadway links across the city, and periodic updates of atmospheric data. The outputs it provides are the estimates of pollution levels on a periodic basis. For a comprehensive review of line source dispersion models, the interested reader may refer to [25] or [26].

In addition to the traffic and weather data inputs, the Gaussian Plume model takes a lot of parameters as inputs, such as the emission factors associated to the roadway links (depending on the composition of the fleet), the pollution dispersion coefficients which are a proxy for modelling the terrain (density of buildings, etc.), and the background pollution levels (pollution that is not traffic induced). Such parameters are typically heterogeneous across cities and justify the use of different parameters, resolutions and physical resolution, hence PDE-based models, for the different meshes M_m under consideration.

3.2 The Implementation

We use Caline 4, the open-source dispersion modelling suite [27, 28], as a PDE solver to solve the Gaussian Plume model for the hourly inputs for each of the 12 domains described above. We note while Caline is one of the “Preferred and Recommended Air Quality Dispersion Model” of the Environmental Protection Agency in the USA [29], it is limited to 20 line sources and 20 receptors per solve, which in turn forces an arbitrary in-homogeneous discretisation of the road network and is another motivation for the use of our deep learning approach.

We have implemented the approach for the use case of Dublin, Ireland. There, the area is partitioned into 12 domains, with 10-20 line sources of pollution each mesh. Time is discretised to hours. For each hour, the inputs to the PDE solver comprise of traffic volume data at each line source, obtained from data aggregation of traffic loop detectors from the SCATS deployment in Dublin, and weather data at a discretisation of the spatial domain, obtained from The Weather Company under a licence: wind speed, wind direction, wind direction standard deviation, temperature, humidity. Available training data comprises almost one year worth of hourly data from July 1st 2017 to April

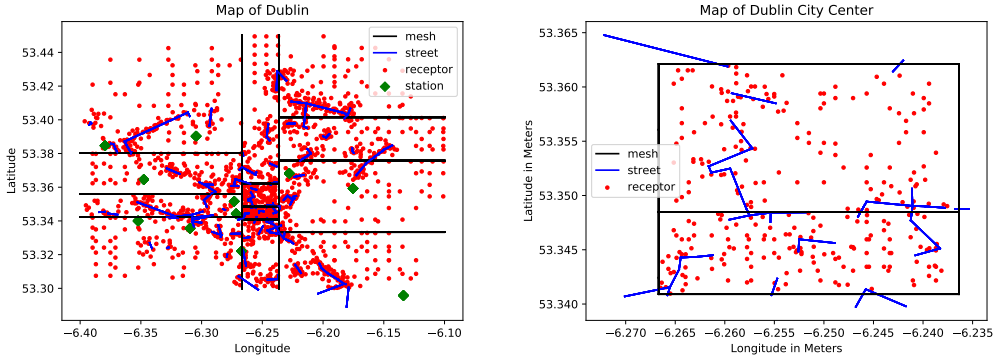


Figure 4: **Left:** Map of Dublin, partitioned into 12 domains (black lines), displaying the positions of line sources (blue lines), receptors (red dots), and measurement stations (green diamonds). **Right:** A close-up of Dublin city center, featuring two partitions with line sources close to boundary.

31st 2018. The outputs include concentrations of NO_2 , $\text{PM}2.5$ and $\text{PM}10$ concentrations at predefined receptors per domain, as suggested in Figure 4. The parameters were chosen for each mesh M_m based on the state-of-the-art practices: the emission factors based on the UK National Atmospheric Emissions Inventory database, dispersion coefficients based on the Caline recommendations (values for inner city, outer city areas), and background pollution levels chosen as the averaged time series values across all pollution measurement stations. The background levels are then replaced by the actual time series data from the time slice averages over the measurement stations. Thus, Caline computes only the traffic and wind contributions to the pollution levels, and this is what we denote as its output.

The RNN model is implemented in Tensorflow [30] to obtain, in effect, the non-linear regression between the inputs and outputs, with the consistency constraints applied iteratively. That is, with each map from the inputs to the outputs, we also obtain further consistency constraints to use in further runs on the same domain. The inputs of the model consist of the Caline inputs at each time step as well as the Caline outputs of the previous time step to take the autocorrelation of the time series data into account. The cost function uses the standard regularisation with the l_2 -loss of the weights with a factor of 10^{-4} . For the consistency constraints we choose $\zeta = 1$ and consider different values for λ and κ . As neural network we choose a multilayer perceptron consisting of six layers, each having 50 nodes, where the input and hidden layers use a ReLU activation, and the output layer uses a linear activation function. We use the Adam optimisation algorithm to train the network with a batch size of 128 over 250 epochs in each iteration.

Using domain knowledge, we could pick ϵ_{mn} specific to $(m, n) \in \mathcal{B}$ based on the expected accuracy of the PDE-based model therein, as it is clear that a better accuracy can be expected when line sources are situated closer to the boundary. It hence would be sensible to consider ϵ_{mn} to be the minimum of 1 and the minimum distance of a line source to the boundary, where 1 corresponds to 100 meters. This choice takes effect not only in the threshold in the inequality 1, but via the construction of $\bar{\chi}_{p_1, p_2 i}$ and $\underline{\chi}_{p_1, p_2 i}$, it also affects the ‘‘learning rate’’: the higher the ϵ_{mn} , the faster the consistency constraints adapt to the solution obtained using the model trained on the adjacent tiles. We leave this implementation for future work and set $\epsilon_{mn} = \epsilon = 1$, if not otherwise noted, e.g., in Appendix A.

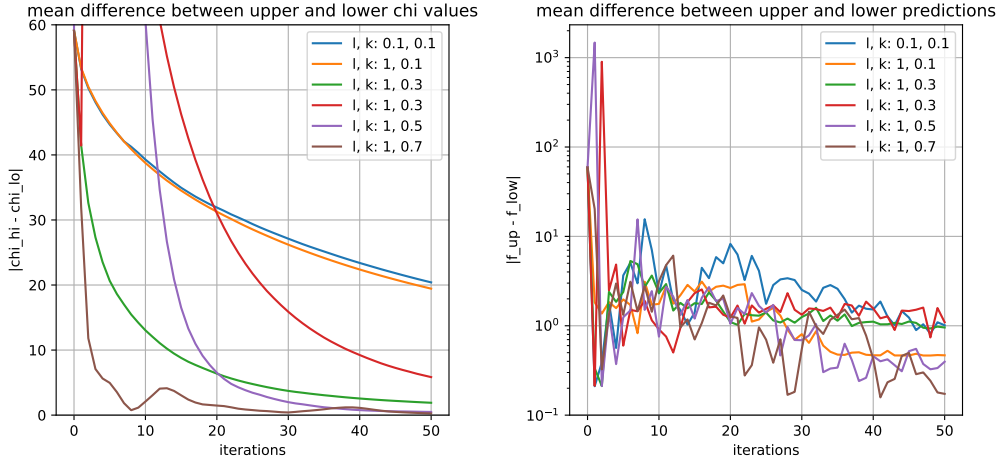


Figure 5: Effects of consistency constraints. **Left:** Mean difference between $\underline{\chi}$ and $\bar{\chi}$ for the boundary between the tiles in the top left. In the legend, l stands for λ , and k stands for κ . **Right:** Mean difference between the learned model predictions at the boundary from the two neighbouring tiles in the top left, with consistency constraints.

4 Results

For validation purposes, we have used hourly NO_2 concentrations measured at 6 sites across the city. (There are also 9 stations providing PM concentrations.) Figure 4 illustrates their positions, and Figure 6 illustrates the performance of the deep-learning forecaster at one example receptor, collocated with a measurement site used for our validation. The mean absolute error (MAE) of the deep-learning forecast against the CALINE computed values without the consistency constraints was about $0.2 \mu\text{g}/\text{cm}^3$ after four to five iterations, which was increased to $0.6 \mu\text{g}/\text{cm}^3$ using the consistency constraints. It should be noted that the consistency constraints plausibly increases error between individual subdomains and the test data as it introduces information external to the domain to smooth physical discontinuities. Those numbers have to be compared to the average of the background pollution levels, which is $21.6 \mu\text{g}/\text{cm}^3$. Thus, for forecasting purposes, we achieved an accuracy of 1 per cent without constraints, and 3 per cent with constraints. This is clearly because the same number of parameters have to fit an increased number of constraints. However, comparing the predictions of the models at the locations of the measurement stations, we can observe a decrease of the errors by up to 50 per cent for the model with the consistency constraints compared to the one without.

Figure 5 shows a few interesting cases for the boundary between the city center tiles: for $\kappa = 0.1$, we observe a slightly better convergence of the constraints interval $(\underline{\chi}, \bar{\chi})$ for higher values of λ , that is a stronger contribution of the consistency constraints to the cost function. Likewise, increasing κ , we observe faster convergence. The difference between the two $\kappa = 0.3$ lines is due to the non-convexity of the problem, which sometimes leads to sudden increases in the interval and correspondingly an increase in the differences between the trained model outputs of the neighbouring tiles (c.f. the first few iterations of the right plot). For $\kappa = 0.7$ we start to enter the oscillatory regime, which can be clearly observed for even higher values of κ . This is an expected behaviour for strong enough momentum terms added to the gradient decent. As the right plot also shows, after 50 iterations, the boundary artefacts practically disappeared as they are of the order of the MAE.

Comparing the performance of the Caline model with the trained RNN model, we observe a

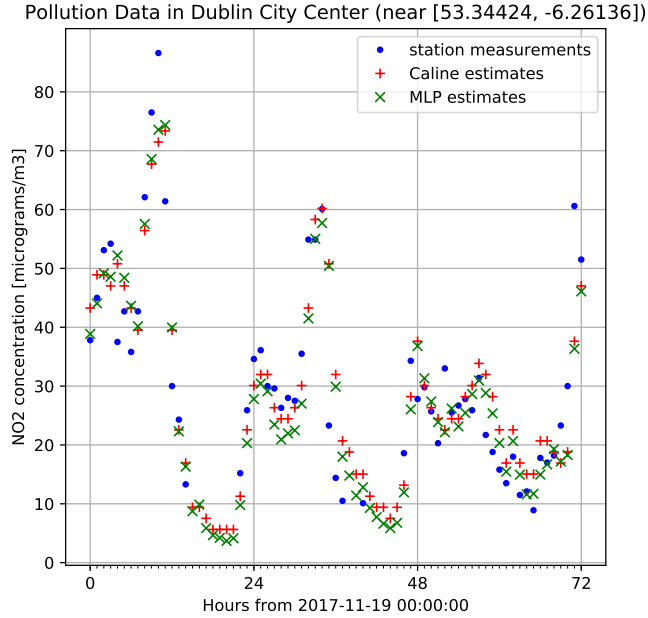


Figure 6: Output at one sample receptor collocated with a sensor over 3 days. The MLP output is taken after three iterations of training with $\lambda = 1$ and $\kappa = 0.5$ and all other parameters as specified in the text.

speedup of a factor of about 6,000 in the model application to the year worth of data from the Dublin area.

5 Conclusions

We have presented consistency constraints, which make it possible to train DNN on small domains and apply the trained models to larger domains while allowing incorporation of information external to the domain. The consistency constraints will ensure the solutions are physically meaningful even at the boundary of the small domains in the output of the DNN. We have demonstrated promising results on an air-pollution forecasting model for Dublin, Ireland.

The work is a first that makes possible numerous extensions. First, one could consider further applications of the consistency constraints, e.g., in energy conservation, or in consider merging the outputs of a number of PDE models within multi-physics applications. Second, in some applications, it may be useful to explore other network topologies. Following [16], one could use long short-term memory (LSTM) units. Further, over-fitting control could be based on an improved stacked auto-encoder architecture [31]. In interpretation of the trained model, the approach of [32] may be applicable. One could also consider applications to inverse problems, following [33, 34].

Our work could also be seen as an example of Geometric Deep Learning [35], especially in conjunction with the use of mesh-free methods [36], such as the 3D point clouds [37], non-uniform meshing, or non-uniform choice of receptors within the meshes. Especially for applications, where the grids are in 3D or higher dimensions, the need for such techniques is clear. More generally, one could explore links to isogeometric analysis of [38], which integrates solving PDEs with geometric

modelling.

Finally, one could generalise our methods in a number of directions of the multi-fidelity [20] modelling, e.g., by combining the reduced-order and full-order models using adaptation, fusion, or filtering. Overall, the scaling up of deep learning for PDE-based models seems to be a particular fruitful area for further research.

Within the domain of our example application, recent surveys [11] suggest that ours is the first use of deep learning in the forecasting of air pollution levels. Following the copious literature on PDE-based models of air pollution, one could consider further pollutants such as ground-level ozone concentrations [39], and ensemble [40] or multi-fidelity methods. One may also consider a joint model, allowing for traffic forecasting, weather forecasting, and air pollution forecasting, within the same network, possibly using LSTM units [32], at the same time.

References

- [1] P. Benner, S. Gugercin, and K. Willcox, “A survey of projection-based model reduction methods for parametric dynamical systems,” *SIAM Review*, vol. 57, no. 4, pp. 483–531, 2015.
- [2] I. Goodfellow, Y. Bengio, and A. Courville, *Deep learning*. Cambridge, MA: MIT Press, 2016.
- [3] I. E. Lagaris, A. Likas, and D. I. Fotiadis, “Artificial neural networks for solving ordinary and partial differential equations,” *IEEE Transactions on Neural Networks*, vol. 9, no. 5, pp. 987–1000, Sept 1998.
- [4] I. E. Lagaris, A. C. Likas, and D. G. Papageorgiou, “Neural-network methods for boundary value problems with irregular boundaries,” *IEEE Transactions on Neural Networks*, vol. 11, no. 5, pp. 1041–1049, Sept 2000.
- [5] H. Lee and I. S. Kang, “Neural algorithm for solving differential equations,” *Journal of Computational Physics*, vol. 91, no. 1, pp. 110–131, 1990.
- [6] P. Ramuhalli, L. Udpa, and S. S. Udpa, “Finite-element neural networks for solving differential equations,” *IEEE Transactions on Neural Networks*, vol. 16, no. 6, pp. 1381–1392, Nov 2005.
- [7] J. Delpiano and P. Zegers, “Semi-autonomous neural networks differential equation solver,” in *The 2006 IEEE International Joint Conference on Neural Network Proceedings*, July 2006, pp. 1863–1869.
- [8] G. D. Muro and S. Ferrari, “A constrained backpropagation approach to solving partial differential equations in non-stationary environments,” in *2009 International Joint Conference on Neural Networks*, June 2009, pp. 685–689.
- [9] K. Rudd, G. D. Muro, and S. Ferrari, “A constrained backpropagation approach for the adaptive solution of partial differential equations,” *IEEE Transactions on Neural Networks and Learning Systems*, vol. 25, no. 3, pp. 571–584, March 2014.
- [10] K. Rudd, “Solving partial differential equations using artificial neural networks,” Ph.D. dissertation, 2013.
- [11] C. Bellinger, M. S. M. Jabbar, O. Zaïane, and A. Osornio-Vargas, “A systematic review of data mining and machine learning for air pollution epidemiology,” *BMC public health*, vol. 17, no. 1, p. 907, 2017.

[12] A. Karpatne, G. Atluri, J. H. Faghmous, M. Steinbach, A. Banerjee, A. Ganguly, S. Shekhar, N. Samatova, and V. Kumar, “Theory-guided data science: A new paradigm for scientific discovery from data,” *IEEE Transactions on Knowledge and Data Engineering*, vol. 29, no. 10, pp. 2318–2331, 2017.

[13] R. Swischuk, L. Mainini, B. Peherstorfer, and K. Willcox, “Projection-based model reduction: Formulations for physics-based machine learning,” *Computers and Fluids*, 2018.

[14] J. Tompson, K. Schlachter, P. Sprechmann, and K. Perlin, “Accelerating Eulerian fluid simulation with convolutional networks,” in *Proceedings of the 34th International Conference on Machine Learning*, ser. Proceedings of Machine Learning Research, D. Precup and Y. W. Teh, Eds., vol. 70. International Convention Centre, Sydney, Australia: PMLR, 06–11 Aug 2017, pp. 3424–3433.

[15] S. C. James, Y. Zhang, and F. O’Donncha, “A machine learning framework to forecast wave conditions,” *Coastal Engineering*, vol. 137, pp. 1–10, 2018.

[16] S. Wiewel, M. Becher, and N. Thuerey, “Latent-space physics: Towards learning the temporal evolution of fluid flow,” *arXiv preprint arXiv:1802.10123*, 2018.

[17] J. Gergonne, “The application of the method of least squares to the interpolation of sequences,” *Historia Mathematica*, vol. 1, no. 4, pp. 439–447, 1974.

[18] S. Boyd and L. Vandenberghe, *Convex optimization*. Cambridge university press, 2004.

[19] M. Mevissen, M. Kojima, J. Nie, and N. Takayama, “Solving partial differential equations via sparse sdp relaxations,” *Pacific Journal of Optimization*, vol. 4, no. 2, pp. 213–241, 2008.

[20] B. Peherstorfer, K. Willcox, and M. Gunzburger, “Survey of multifidelity methods in uncertainty propagation, inference, and optimization,” *SIAM Review*, vol. 60, no. 3, pp. 550–591, 2018.

[21] G. Cybenko, “Approximation by superpositions of a sigmoidal function,” *Mathematics of Control, Signals and Systems*, vol. 2, no. 4, pp. 303–314, Dec 1989.

[22] A. Quarteroni and A. Valli, “Domain decomposition methods for partial differential equations numerical mathematics and scientific computation,” *Quarteroni, A. Valli–New York: Oxford University Press.–1999*, 1999.

[23] W. H. Organization, *Burden of disease from household air pollution for 2016*.

[24] O. Sutton, “The problem of diffusion in the lower atmosphere,” *Quarterly Journal of the Royal Meteorological Society*, vol. 73, no. 317-318, pp. 257–281, 1947.

[25] S. Nagendra and M. Khare, “Line source emission modelling,” *Atmospheric Environment*, vol. 36, no. 13, pp. 2083 – 2098, 2002.

[26] J. M. Stockie, “The mathematics of atmospheric dispersion modeling,” *SIAM Review*, vol. 53, no. 2, pp. 349–372, 2011.

[27] C. T. at the California Department of Transportation, “Caline4 – a dispersion model for predicting air pollutant concentrations near roadways,” *Report No. FHWA/CA/TL-84/15*, 1989.

[28] S. Samaranayake, S. Glaser, D. Holstius, J. Monteil, K. Tracton, E. Seto, and A. Bayen, “Real-time estimation of pollution emissions and dispersion from highway traffic,” *Computer-Aided Civil and Infrastructure Engineering*, vol. 29, no. 7, pp. 546–558, 2014.

[29] US-EPA. (2018) Air quality dispersion modeling - preferred and recommended models. [Online]. Available: <https://www.epa.gov/scram/air-quality-dispersion-modeling-preferred-and-recommended-models>

[30] M. Abadi *et al.*, “Tensorflow: A system for large-scale machine learning,” in *Proceedings of the 12th USENIX Conference on Operating Systems Design and Implementation*, ser. OSDI’16. Berkeley, CA, USA: USENIX Association, 2016, pp. 265–283.

[31] T. Zhou, G. Han, X. Xu, Z. Lin, C. Han, Y. Huang, and J. Qin, “ δ -agree adaboost stacked autoencoder for short-term traffic flow forecasting,” *Neurocomputing*, vol. 247, pp. 31–38, 2017.

[32] Z. Cui, K. Henrickson, R. Ke, and Y. Wang, “High-order graph convolutional recurrent neural network: A deep learning framework for network-scale traffic learning and forecasting,” *arXiv preprint arXiv:1802.07007*, 2018.

[33] M. Raissi, P. Perdikaris, and G. E. Karniadakis, “Machine learning of linear differential equations using gaussian processes,” *Journal of Computational Physics*, vol. 348, pp. 683 – 693, 2017.

[34] M. Raissi and G. E. Karniadakis, “Hidden physics models: Machine learning of nonlinear partial differential equations,” *Journal of Computational Physics*, vol. 357, pp. 125 – 141, 2018.

[35] M. M. Bronstein, J. Bruna, Y. LeCun, A. Szlam, and P. Vandergheynst, “Geometric deep learning: Going beyond euclidean data,” *IEEE Signal Processing Magazine*, vol. 34, no. 4, pp. 18–42, July 2017.

[36] J. Sirignano and K. Spiliopoulos, “Dgm: A deep learning algorithm for solving partial differential equations,” *arXiv preprint arXiv:1708.07469*, 2017.

[37] C. R. Qi, L. Yi, H. Su, and L. J. Guibas, “Pointnet++: Deep hierarchical feature learning on point sets in a metric space,” in *Advances in Neural Information Processing Systems*, 2017, pp. 5099–5108.

[38] J. A. Cottrell, T. J. Hughes, and Y. Bazilevs, *Isogeometric analysis: toward integration of CAD and FEA*. John Wiley & Sons, 2009.

[39] V. Mallet, A. Nakonechny, and S. Zhuk, “Minimax filtering for sequential aggregation: Application to ensemble forecast of ozone analyses,” *Journal of Geophysical Research: Atmospheres*, vol. 118, no. 19, 2013.

[40] V. Mallet, “Ensemble forecast of analyses: Coupling data assimilation and sequential aggregation,” *Journal of Geophysical Research: Atmospheres*, vol. 115, no. D24, 2010.

[41] D. Fernández and M. Solodov, “Stabilized sequential quadratic programming for optimization and a stabilized newton-type method for variational problems,” *Mathematical Programming*, vol. 125, no. 1, pp. 47–73, Sep 2010. [Online]. Available: <https://doi.org/10.1007/s10107-008-0255-4>

[42] P. E. Gill, V. Kungurtsev, and D. P. Robinson, “A stabilized sqp method: superlinear convergence,” *Mathematical Programming*, vol. 163, no. 1, pp. 369–410, May 2017. [Online]. Available: <https://doi.org/10.1007/s10107-016-1066-7>

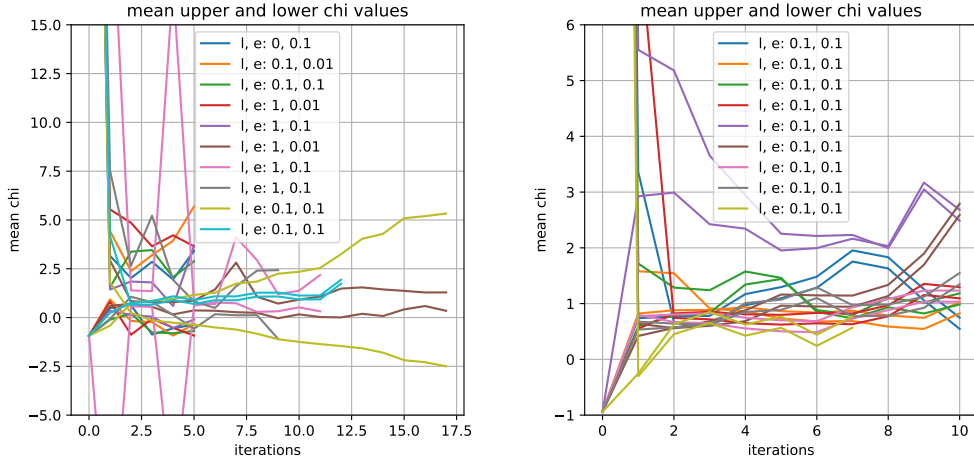


Figure 7: Mean values for $\underline{\chi}$ and $\bar{\chi}$ for the boundary between the city center tiles of figure 5. In the legend, l stands for λ , and e for ϵ . **Left:** based on equation 5. **Right:** based on equation 6.

A Alternative Iterative Update Approaches

As discussed earlier, equation 3 is not the most naïve version to update the boundary constraints. A much easier and direct version is to consider

$$\underline{\chi}_{p_1, p_2, i}^{(k+1)} = \min(f_{p_1, t_i}^{(m)}, f_{p_2, t_i}^{(n)}) + \epsilon_{mn}, \quad \bar{\chi}_{p_1, p_2, i}^{(k+1)} = \max(f_{p_1, t_i}^{(m)}, f_{p_2, t_i}^{(n)}) - \epsilon_{mn}. \quad (5)$$

This prescription however does not guarantee convergence of the constraints interval at all, as can be seen in left of figure 7. Likewise, it does leave to convergence of the trained model predictions at the boundaries of the mesh. In order to ensure convergence of the constraint interval, we can implement it by design, such as

$$\begin{aligned} \underline{\chi}_{p_1, p_2, i}^{(k+1)} &= \max\left(\min\left(f_{p_1, t_i}^{(m)}, f_{p_2, t_i}^{(n)}\right), \min\left(\underline{\chi}_{p_1, p_2, i}^{(k)}, \max\left(f_{p_1, t_i}^{(m)}, f_{p_2, t_i}^{(n)}\right)\right)\right) + \epsilon_{mn}, \\ \bar{\chi}_{p_1, p_2, i}^{(k+1)} &= \min\left(\max\left(\min\left(f_{p_1, t_i}^{(m)}, f_{p_2, t_i}^{(n)}\right), \bar{\chi}_{p_1, p_2, i}^{(k)}\right), \max\left(f_{p_1, t_i}^{(m)}, f_{p_2, t_i}^{(n)}\right)\right) - \epsilon_{mn}. \end{aligned} \quad (6)$$

With each iteration, this interval shrinks to a minimum size of $2\epsilon_{mn}$, as can be seen in the right of figure 7, where the intervals reach size 0.2 after a few iterations. We also note though this does not ensure convergence of the actual values. It is well-known that Lagrangian methods for non-linear optimisation benefit tremendously from stabilisation [41, 42]. Hence, we chose the stabilised method in equation 3, which includes a shift term similar to the process in equation 6, but with vanishing strength for later iterations. Adding the gradient term replaces the ϵ_{mn} contribution, which is recovered again by multiplying it to the Lagrangian parameter λ .